Mechanical loss, creep, diffusion and ionic conductivity of ZrO_2-8 mol%Y_2O_3 polycrystals

A. Lakki [a,1], R. Herzog [a,2], M. Weller [a,*], H. Schubert [b], C. Reetz [b],
O. Görke [b], M. Kilo [c], G. Borchardt [c]

[a]*Max-Planck-Institut für Metallforschung, Seestr. 92, D-70174 Stuttgart, Germany*
[b]*Technische Universität Berlin, Institut für Nichtmetallisch-Anorganische Werkstoffe Englische Str. 20, D-10587, Berlin, Germany*
[c]*Technische Universität Clausthal, Metallurgisches Zentrum, AG Elektronische Materialien, Robert-Koch-Str. 42, D-38678 Clausthal-Zellerfeld, Germany*

Abstract

Polycrystalline ZrO_2-8 mol%Y_2O_3 was investigated by combining several experimental techniques on identical materials sintered out of the same high purity powder. The mechanical loss spectrum (damping and elastic modulus) was measured in a large frequency and temperature range (10^{-2}Hz–1.5kHz; −150 to 1400°C). Damping due to point defect relaxation at low temperature and to viscoelastic relaxation at high temperature was revealed. The creep resistance was investigated with four-point bending tests (stress and temperature ranges: 20–75 MPa, 1100–1290°C), indicating Nabarro-Herring creep as the main rate-controlling mechanism. Both viscoelastic deformation and creep seem to be controlled by cation diffusion. Measurements of the ^{96}Zr tracer diffusivity by secondary ion mass spectrometry at 1125–1460°C yielded an activation enthalpy of 460 kJ/mol. Close values were obtained for creep (440 kJ/mol) and viscoelastic relaxation (530 kJ/mol). Finally, the ionic DC-conductivity of these electrolytes was measured with high accuracy in the range 300–1250°C. © 2000 Elsevier Science Ltd. All rights reserved.

Keywords: Mechanical properties; Creep; Diffusion; Ionic conductivity; ZrO_2

1. Introduction

Because of its high oxygen conductivity, stabilized zirconia is of technological interest for fuel cells.[1,2] Especially ZrO_2-8 mol%Y_2O_3 is a preferred candidate for the solid electrolyte.[3] As the electrical conductivity relies on the diffusion of oxygen vacancies, such cells operate at high temperatures (typically 1000°C). However, already at these temperatures, cation diffusion becomes of importance.[4–6] This results in degradation of both the mechanical properties (creep)[7] and the electrical properties (ageing),[3,8] the mechanisms of which are not yet fully understood. Recent investigations on the zirconium tracer diffusivity in single crystals indicate that cation diffusion takes place via cation vacancies. Nevertheless, the kind of vacancies and their formation

mechanism are not yet clear.[6] Even the complex phase equilibria in these materials having compositions near the cubic/cubic + tetragonal phase boundary are not unambiguously established[9–11] and metastable phase diagrams are often used.[12] As to the creep properties of high-purity polycrystalline ZrO_2-8 mol%Y_2O_3, little information is available. Most of the reported investigations on creep of yttria-stabilized cubic polycrystalline zirconia refer to impure, porous, partially stabilized or higher doped materials.[13–20] Moreover, the high-temperature damping properties of these materials are poorly known, mainly due to technical difficulties in measuring mechanical loss spectra at high temperature. Finally, any investigation of the above properties is limited by the influence of microstructural parameters (impurities, grain size and morphology, phase partitioning) and thermal history.

In order to overcome such uncertainties, we performed all measurements on well characterized, identical materials, sintered out of the same high purity powder. The mechanical and electrical properties were investigated by a combination of experimental techniques: mechanical spectroscopy, four-point bending

creep tests, cation tracer diffusion measurements using secondary ion mass spectrometry (SIMS) and four-electrode DC-conductivity measurements (Fig. 1).

2. Experimental procedure

2.1. Materials processing and characterization methods

One single batch (No Z804152P) of commercial high purity binder-free ZrO_2-8 mol%Y_2O_3 powder was used (TZ-8Y, Tosoh Corp., Japan). The dopant and impurity contents determined by Inductively Coupled Plasma-Optical Emission Spectrometry (ICP-OES) analysis are given in Table 1 (producer's specifications). The powders were compacted at room temperature first uni-axially (20 MPa) and then isostatically (300 MPa). They were subsequently sintered at 1600°C for 2 h in air; the heating and cooling rates were 1 and 3 K/min respectively. Some materials sintered at 1480 and 1420°C were also produced. A more detailed description of the materials processing and characteristics is given elsewhere.[21]

Grain size determination of the sintered materials was carried out by image analysis of scanning electron microscopy (SEM) micrographs obtained on polished, thermally etched surfaces. Samples were diamond-cut out of the sintered slabs. A few samples were further annealed in air.

X-ray analysis was performed with a Siemens D5000 diffractometer equipped with a position sensitive detector and with a Siemens D500, both using CuK_α radiation. The conditions were: acceleration voltage 40 kV, current 50 mA, step size 0.02–0.05 deg, sampling time 5–20 s.

Transmission electron microscopy (TEM) observations were carried out with a JEOL-2000FX instrument with EDX facility and with a Zeiss EM 912 Omega instrument with energy filtering, operated at 200 and 120 kV, respectively, using a double-tilt sample holder. Samples were prepared by grinding, dimpling and ion milling and subsequently coated with carbon, to avoid charging. Selected Area Diffraction (SAD) and dark field imaging were used to investigate tetragonal phase contrast.

Raman spectroscopy measurements were performed in a Bruker IFS88 instrument, combined with a FRA106
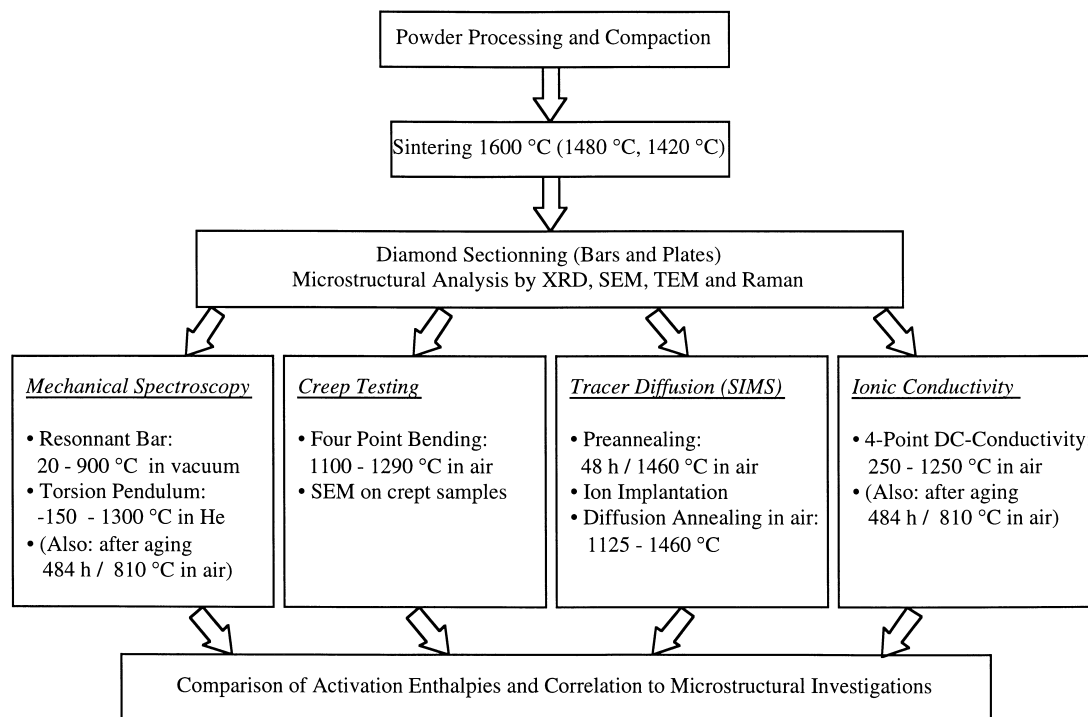

Fig. 1. Overview of the experimental techniques used and measuring conditions.

Table 1
Dopant and impurity content of the TZ-8Y powders (measured by ICP-OES) and of the sintered body (measured by XRF)

	Dopant/impurity content	Y_2O_3	Al_2O_3	SiO_2	Fe_2O_3	Na_2O
Powder	[wt%]	13.380	0.005	0.004	0.006	0.078
	[mol%]	7.8				
Sintered body	[mol%]	8.6				

Raman accessory. The 1076 nm line of a Nd:YAG laser was used for excitation. Usually 100 scans were accumulated to obtain a good signal/noise ratio. Spectra were recorded in reflection from the polished sample surfaces. The samples were previously annealed in air for: 100 days/1150°C, 7 days/1460°C and 12 h/1700°C.

2.2. Mechanical spectroscopy

Mechanical spectroscopy consists in measuring the fractional dissipation of energy per vibration cycle due to the motion of structural defects[25], as a function of frequency or temperature. The present investigations explored different temperature and frequency ranges by using three different apparatuses briefly presented in the following (for details see the cited references). Samples of typically $43 \times 5 \times 0.6$–1.2 mm^3 size were cut from the sintered slabs. The measurements were carried out in a 10 mbar He atmosphere or in vacuum, during heating.

(a) *Free-decay inverted torsion pendulum* (range: 1–20 Hz, −150 to 700°C):[22] A sample is mounted vertically, one end being gripped and the other excited to free torsional vibrations. The logarithmic decrement ϑ of the decaying vibration amplitude and the frequency f are recorded. From these, the internal friction (damping), which represents the inverse quality factor Q^{-1}, or loss tangent, can be calculated from the logarithmic decrement, ϑ, using the formula:

$$Q^{-1} = \frac{\vartheta}{\pi}\left(1 - \frac{\vartheta}{2\pi} + \ldots\right) \tag{1}$$

The second term in Eq. (1) corrects for the anharmonicity of the damped oscillations. The dynamical (i.e. frequency-dependent) torsion modulus G is proportional to f^2, $G \propto f^2$. Its absolute value can be determined by comparing with a specimen of known modulus (same inertia of the pendulum).

(b) *Resonant bar apparatus* (range: 1–3 kHz, 0–900°C):[23] A sample is mounted horizontally and excited to free-free flexural oscillations. Q^{-1} and the dynamical Young's modulus $E \propto f^2$ are obtained similarly as under (a).

(c) *Forced-vibration inverted torsion apparatus* (range: 10^{-4}–10 Hz, 0–1400°C):[24] Similar as in (a), but without inertia and with imposed constant frequency. Two signals are compared by the frequency generator-analyzer unit, corresponding to the applied torque and to the angle of deformation. From the phase lag ϕ and the amplitude ratio, the mechanical loss $\tan\phi \equiv Q^{-1}$ and the relative variation of G are obtained.

Two types of relaxation phenomena which are frequently encountered by mechanical spectroscopy and which are of relevance for the present paper are briefly presented:

(i) *Anelastic relaxation*. The mechanical loss shows a (Debye) peak for which the internal friction is given by:

$$Q^{-1} = \Delta \frac{\omega\tau}{1 + \omega^2\tau^2}. \tag{2}$$

where $\Delta = 2Q_{\max}^{-1}$ is the relaxation strength (depending on the defect concentration), $\omega = 2\pi f$ is the cyclic frequency of vibration and τ is the relaxation time. In parallel, the dynamical elastic modulus shows a decrease. Often τ follows Arrhenius-type behaviour:

$$\tau = \tau_\infty \exp(H_{\mathrm{MS}}/kT) \tag{3}$$

where τ_∞^{-1} is the attempt frequency, H_{MS} is the activation enthalpy of the underlying mechanism of mechanical loss and k is the Boltzmann factor. H_{MS} can be determined from the shift of the peak with freqency.

(ii) *Viscoelastic relaxation*. The mechanical loss shows a monotonic increase ("background") with temperature, while the dynamical elastic modulus decreases steadily in parallel. According to the model by Schoeck et al.,[26] the high-temperature damping background can often be described by the following phenomenological relation:

$$\tan\phi = \frac{1}{(\omega\tau)^\alpha} \tag{4}$$

where and $1/\alpha$ is a broadening factor due, e.g. to a distribution of relaxation times. For thermally activated relaxation [Eq. (3)] and $\omega = 2\pi f$ it follows:

$$\tan\phi = \frac{A}{f^{\bar{\alpha}}} \exp(-\alpha H_{\mathrm{MS}}/kT) \tag{4a}$$

where A is a constant.

2.3. Four-point bending creep tests

The constant load creep tests were carried out in a four-point bending apparatus (type 422 E 4, Netzsch-Gerätebau GmbH, Germany). The displacement was measured using a linear voltage differential transducer in contact with the sample and the resulting deformation was calculated on-line. Samples of $45 \times 5 \times 4$ mm^3 were cut from the sintered slabs and the edges were rounded off. The specimens were mounted under a minimal load of 4 N and heated to the test temperature at 5 K/min. After thermal equilibration of 30 min, one creep test per sample was performed, lasting 20 h. The stress and temperature range was 20–75 MPa and 1100–1290°C respectively.[21]

The steady-state creep rate ($\dot{\epsilon}$) data were evaluated with the usual equation:[7]

$$\dot{\epsilon} = A' \frac{\sigma^n}{d^p} \exp(-H_{\mathrm{creep}}/kT) \tag{5}$$

where A' is a constant, σ the applied stress, n the stress exponent, d the grain size, p the grain size parameter, and H_{creep} the activation enthalpy.

2.4. Cation diffusion experiments

Samples of $10\times10\times1$ mm^3 size were cut and polished with the alumina suspension "Final" (particle size 500 nm). In order to heal near-surface defects induced during polishing, the samples were preannealed for 2 days at about 1460°C in air and rapidly cooled. For the cation diffusion experiments, a thin layer (20 nm) of ZrO$_2$ containing 59.6% ^{96}Zr (natural isotopic abundance: 2.8%) was applied onto the surface. Diffusion occured by annealing at temperatures between 1125 and 1460°C in air, followed by rapid cooling.

The diffusion profiles were obtained through the depth profile analysis method, using a VG SIMS-Lab at the Ecole des Mines, Nancy, France. An Ar$^+$ primary ion beam with an energy of 8 keV was used for excitation and a flood gun was necessary to reduce sample charging. The ion beam was scanned over a sample area of $<0.5\times0.5$ mm^2. Singly charged secondary ions (cations) were detected. An electronic gating of 30% in each direction was applied to reduce crater effects. To convert sputter time into eroded depth the crater depth was measured using a profilometer. More details are given elsewhere.[6]

Tracer diffusivities D were determined by fitting the appropriate solution of Fick's second law[27] to the tracer isotope concentration profile:

$$c(x, t) - c_0 = 0.5(c_s - c_0) \times (\text{erf}((x + l)/2(Dt)^{0.5})$$

$$- \text{erf}((x - l)/2(Dt)^{0.5})) \tag{6}$$

where c_0 and c_s are the natural and the initial concentration of the tracer isotope, respectively, l is the initial thickness of the tracer layer and t is the diffusion time.

2.5. Electrical resistivity measurements

The ionic DC-conductivity was measured using the four-probe technique in the temperature range 250–1250°C. Conductivity samples (typically $5\times5\times22$ mm^3) were diamond cut. The two small faces (current electrodes) were coated with platinum paste and spring loaded between slides of platinum mesh, in order to enable sufficient oxygen flow. The voltage electrodes had the form of platinum wire loops wrapped around the sample at two equipotential planes at 8mm distance, with platinum paste ensuring good electrical contact. Positive and negative polarity was set for each current value.

3. Results

3.1. Microstructure

The sintering behaviour of the powders was followed by dilatometry, showing nearly complete densification already at ≈1400°C. To obtain different grain sizes, three sintering temperatures were selected (1420, 1480 and 1600°C). All the sintered materials reached almost full density ($\rho > 99\%$ theoretical density). Only a small amount of pores was detected by SEM, decreasing with sintering temperature. Therefore, mainly the material sintered at 1600°C was investigated. A typical micrograph is shown in Fig. 2 (grain size 6.8 µm). Materials with grain sizes 3.9 and 2.4 µm were used for creep tests only. X-ray fluorescence (XRF) analysis yielded a dopant concentration of 8.6 mol%Y$_2$O$_3$ (Table 1).
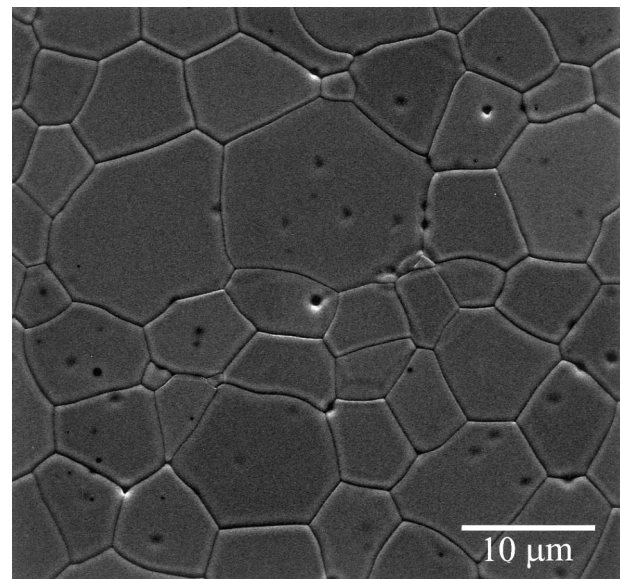

Fig. 2. SEM-micrograph of the investigated ZrO$_2$-8mol% Y$_2$O$_3$ material. Grain size $d=6.8$ µm.
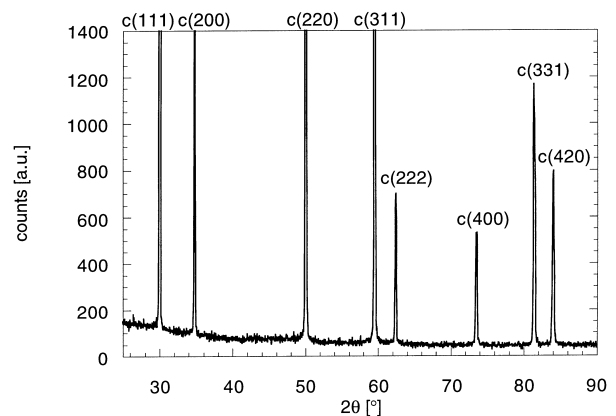

Fig. 3. X-ray spectra of the sintered material. In all cases only cubic (fluorite) reflections are present.

X-ray spectra show all the reflections of the cubic fluorite structure (Fig. 3). No evidence of tetragonal phase was found, i.e. no splitting of the higher order reflections was observed.

Bright field TEM observations showed that the material contains very little visible second phase in the form of spherical inclusions inside the grains or pockets at grain boundaries [Fig. 4(a)]. EDX measurements on several such inclusions revealed the presence of Si, suggesting that they are amorphous. EDX measurements of the Zr/Y ratio on several grains yielded values between 8 and 9 mol%Y_2O_3, consistent with those from chemical analysis (Table 1).

TEM-SAD patterns showed reflections of the (112)-type, forbidden in the cubic fluorite phase and characteristic of the tetragonal phase [Fig. 4(c)]. Moreover, strong diffuse scattering was observed [Fig. 4(c, d)]. A dark-field image of a cubic grain slightly tilted from the [111] zone axis, obtained using a tetragonal (112) reflection, shows a faint contrast on a nanometric scale [Fig. 4(b)].
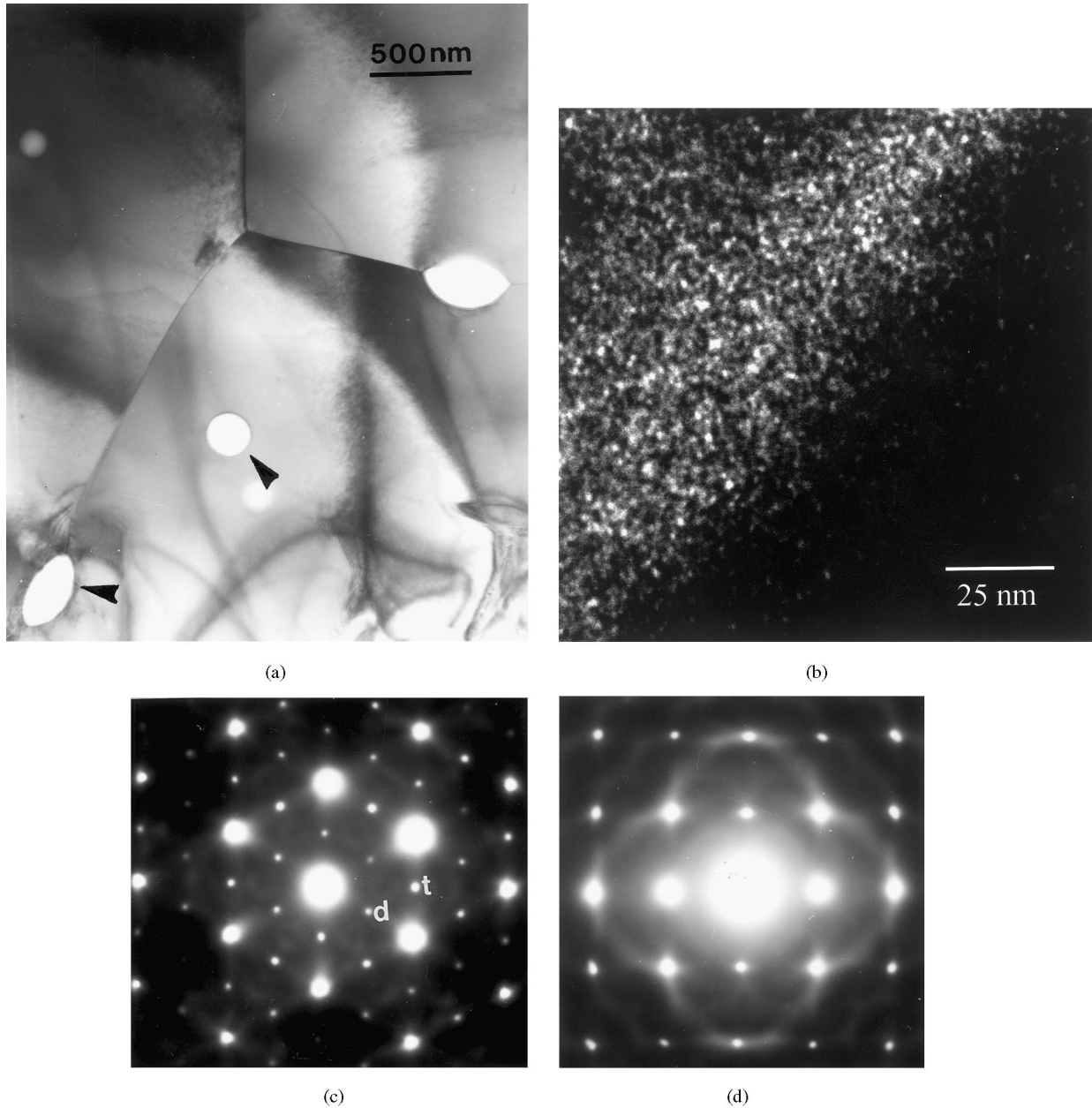

Fig. 4. (a) Bright field electron micrograph of a triple junction in an area containing an untypically high density of glassy phase inclusions and pores. The arrowed inclusions were confirmed by EDX to contain Si. (b) Dark field image of a [111]-oriented grain using a tetragonal (112) reflection. (c) Selected area diffraction pattern of a [111]-oriented grain showing tetragonal reflections (marked *t*), double reflection spots (marked *d*) and diffuse scattering. (d) Selected area diffraction pattern of a grain slightly tilted off the [100] zone axis, showing strong diffuse scattering.

Raman spectroscopy measurements performed on samples annealed at 1150°C showed reflections of both the cubic and the tetragonal phase, while for those annealed at 1460 and 1700°C only the cubic phase was observed (Fig. 5).

3.2. Mechanical spectroscopy

The typical spectrum is shown in Fig. 6, measured with forced vibrations at 0.1Hz. It shows two main components: (a) at low temperature (0–500°C), a double mechanical loss maximum (composed of two sub-maxima designated I and I_B) together with a transition in the dynamical torsion modulus and (b), at high temperature (>900°C), a monotonic increase of the mechanical loss accompanied by a decrease of the modulus. Both are thermally activated relaxation phenomena, since they shift with the vibration frequency.

(i) *Double maximum*. The double maximum was investigated in a large frequency range (0.01 Hz–1.5 kHz). Fig. 7(a and b) shows two examples of measurements using the free decay of oscillations in the torsional and flexural modes, respectively. From the shift of the peak positions with frequency, the activation parameters can be calculated. One so obtains the activation enthalpy and attempt frequency values of, respectively, 135 ± 20 kJ/mol (1.4 ± 0.2 eV), 10^{18} s^{-1} for maximum I and 260 ± 20 kJ/mol (2.7 ± 0.2 eV), 10^{25} s^{-1} for maximum I_B. The maxima are larger than simple Debye maxima [Eq. (2)] by a factor of about 4.
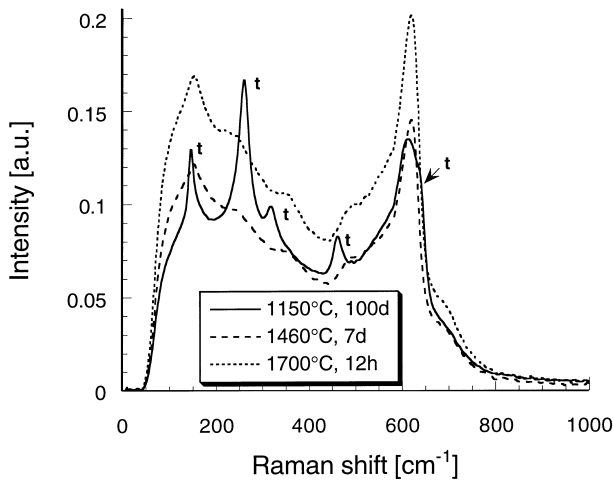

Fig. 5. Raman spectra after ageing (i) 100 days at 1150°C, (ii) 7 days at 1460°C and (iii) 12 h at 1700°C. Features of both the cubic and tetragonal (*t*) phase appear in (i), while only those of the cubic phase are visible in (ii) and (iii).
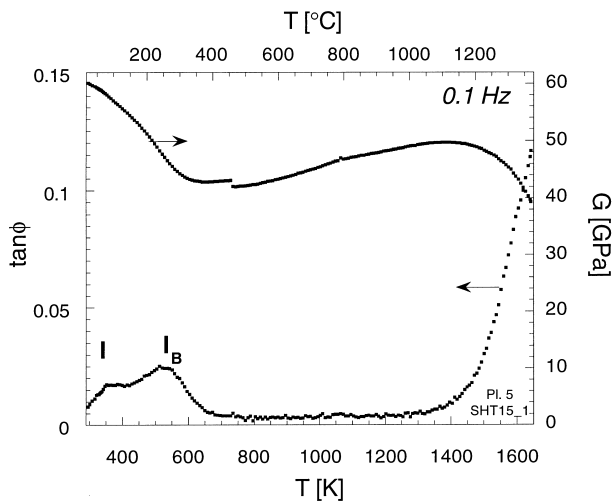

Fig. 6. Typical spectrum (mechanical loss tanϕ and dynamical torsion modulus G) as a function of temperature, measured with forced vibrations at the frequency 0.1 Hz.
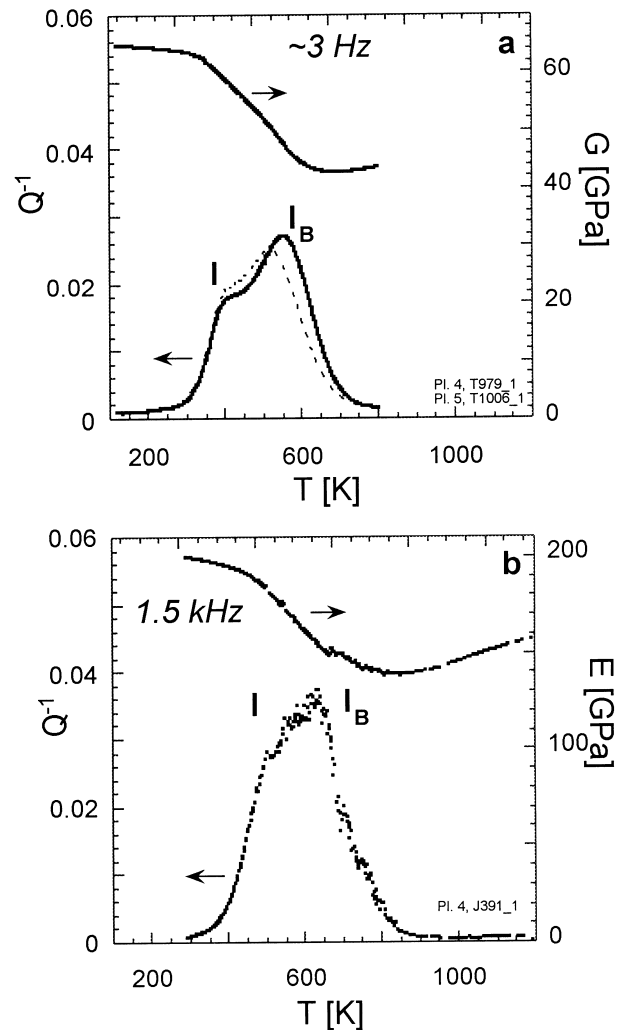

Fig. 7. (a) Low temperature damping Q^{-1} and dynamical torsion modulus G, measured using free decaying torsial vibrations at the frequency of about 3 Hz. The dotted curve shows the spectrum after annealing 484 h at 810°C. (b) Low temperature damping Q^{-1} and dynamical Young's modulus E, measured using free-free flexural vibrations at the frequency of about 1.5 kHz.

After annealing for 484 h at 810°C, the satellite maximum I_B is reduced significantly while maximum I_B remains almost unaffected.

(ii) *Modulus*. Absolute values of the dynamical elastic moduli G and E are given in Fig. 7(a and b) for the torsion and flexural modes. These were obtained by multiplying the square of the measured self-vibration frequency by the appropriate geometrical factors.[22,23] In the case of the measurements under imposed vibrations, the measured relative values of the dynamical modulus can thus also be converted into absolute ones (Fig. 6). At room temperature, $G \approx 65$ GPa and $E = 200$ GPa. At intermediate temperature (500–800°C), one notices an increase of the modulus.

(iii) *High-temperature part*. The monotonic increase of mechanical loss above 900°C (Fig. 6) can be described by Eq. (4). Effectively, on a logarithmic vs inverse temperature representation [Fig. 8(a)], straight lines are obtained. These can be superimposed by shift along the $1/T$ axis, thus producing a linear master spectrum [Fig. 8(b)], typical for viscoelastic deformation. From the shift of the linear segments, an activation enthalpy value (5.7 eV) can be obtained using an Arrhenius diagram [Fig. 8(c)].[28] Double linear regression on all data of Fig. 8(a) to fit the logarithm of Eq. (4) yields $\alpha = 0.3$ and $H_{MS} = 530$ kJ/mol (5.5 eV).

3.3. Creep

A typical creep curve is shown in Fig. 9. After the transient regime (primary creep), steady-state (secondary creep) is reached. The steady-state creep rate can be analyzed by the usual phenomenological equation [Eq. (5)]. Effectively, in Fig. 10(a and b), straight lines are obtained for both $\log \dot{\varepsilon}$ vs $1/T$ and $\log \dot{\varepsilon}$ vs $\log \sigma$. For the material with grain size 6.8 μm, the slopes yield the
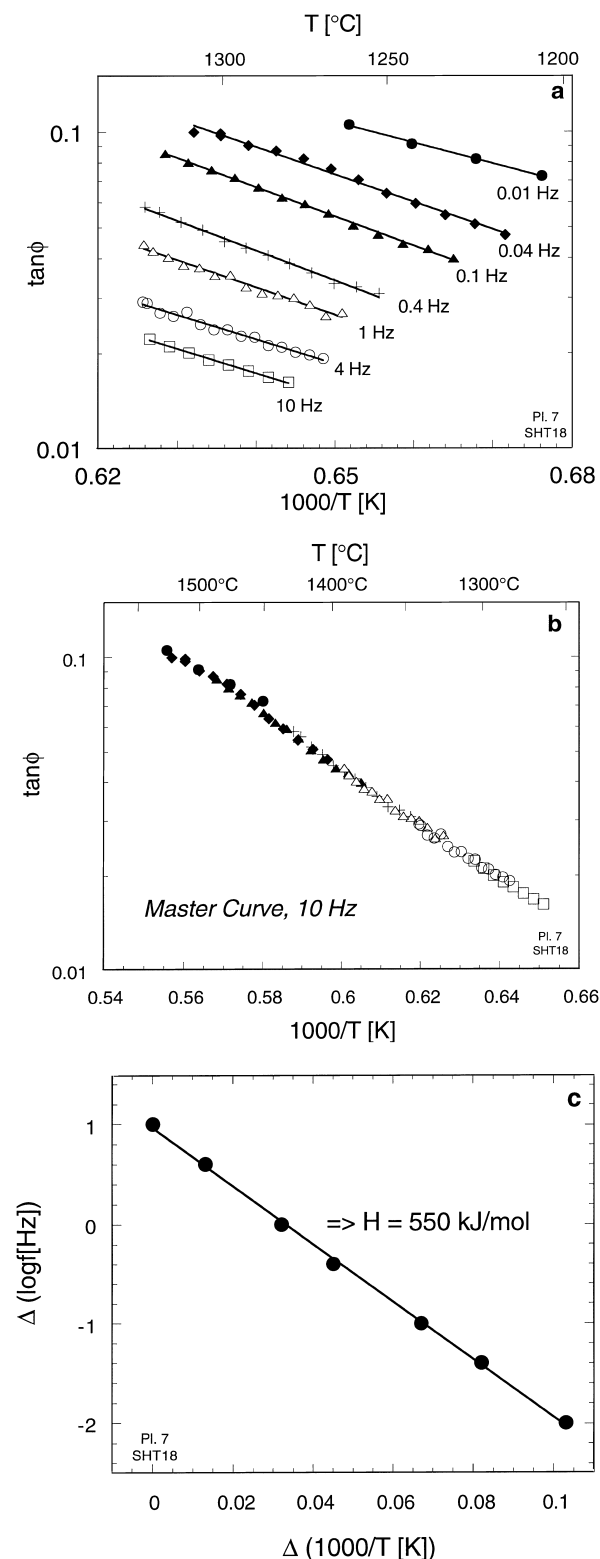

Fig. 8. (a) Shift with measurement frequency of the high-temperature damping. (b) Master spectrum of the high-temperature damping background, obtained by superposing the spectra shown in Fig. 7(a) after shifting them along the $1/T$ axis. (c) Arrhenius diagram reporting the differences of $\log f$ vs the shift along $1000/T$ necessary to superpose the spectra of Fig. 8(b). The slope of the fitted line yields $H_{MS} = 550$ kJ/mol (5.7 eV).
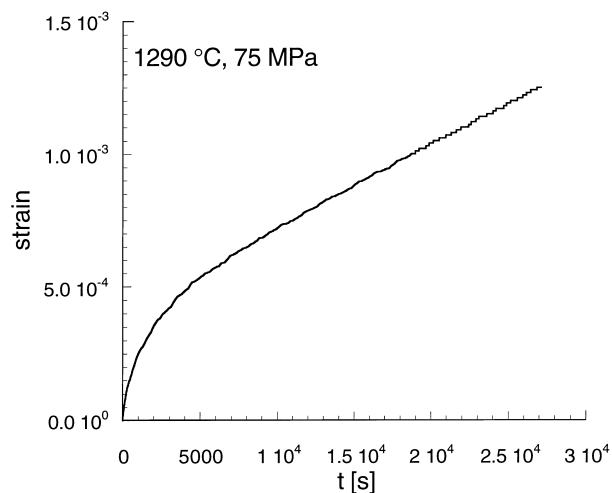
Fig. 9. Typical creep curve (deformation as a function of time), showing the primary (transient) and secondary (steady state) creep stages ($T = 1290$°C, 75 MPa).

values of $n = 1.1 \pm 0.1$ and $H_{creep} = 440 \pm 60$ kJ/mol (4.6 ± 0.6 eV), respectively, for the stress exponent and for the activation enthalpy at 75 MPa. Creep tests on materials made of the same powder but differing only with respect to the grain size confirmed slightly lower values of the activation enthalpy [Fig. 10(a)].[21] By applying multiple linear regression to the whole set of availabe data to fit the logarithm of Eq. (5), one obtains the values of $n \approx 1$, $H = 370$ kJ/mol (3.8 eV) and a grain size parameter of $p \approx 2.5$.

3.4. Cation diffusion

A typical cation concentration profile (^{96}Zr tracer fraction c as a function of the depth x) is reported in Fig. 11. As is shown, it can be fitted quite well by Eq. (6), indicating that only one mechanism of diffusion exists. For the whole temperature range investigated, an Arrhenius-like behaviour is found (Fig. 12). The ^{96}Zr

tracer diffusivity was found to be $D_{Zr} = 0.22$ $\exp(-460 \pm 20$ kJmol^{-1}/kT) cm^2 s^{-1}. This implies fairly large values of the entropy of motion (≈ 5 k$_B$).

3.5. Electrical resistivity

The DC-conductivity is shown in Fig. 13 in an Arrhenius representation. A gradual decrease of slope is observed in the investigated temperature range, corresponding to activation enthalpy values H_{DC} ranging between 110 and 70 kJ/mol ($1.14-0.72$ eV) at low and high temperatures, respectively. The temperature dependence of the activation enthalpy is obtained by local derivation of the σT vs $1/T$ curve. Above 800°C, the derived curve is not smooth, indicating anomalous temperature change of the conductivity. After annealing

Fig. 11. Experimental and fitted [according to Eq. (6)] ^{96}Zr depth profile after annealing 14.2 h at 1428°C.
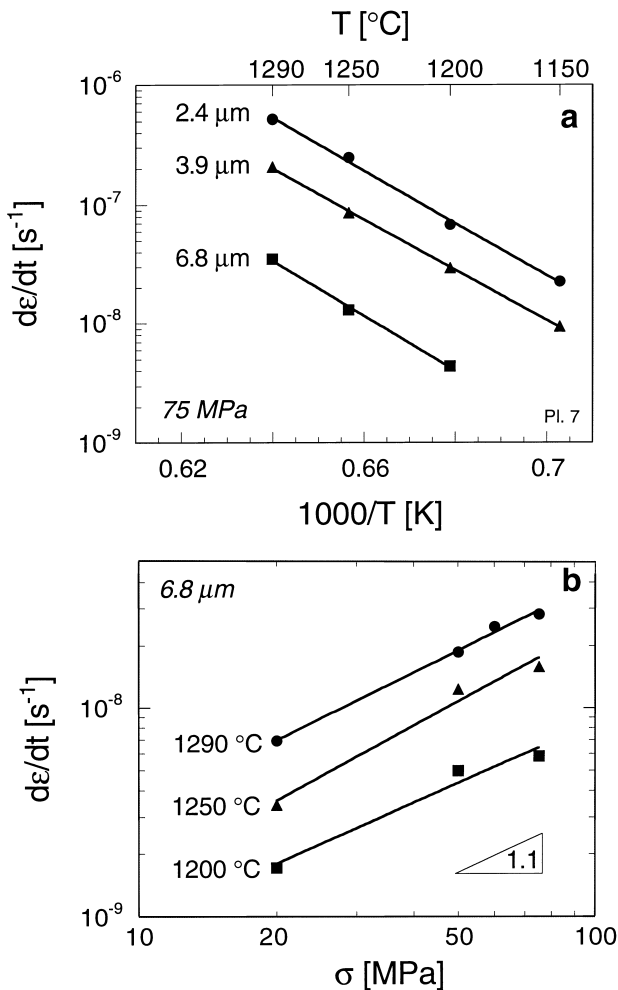

Fig. 10. (a) Temperature dependence of the steady state creep rate at 75 MPa for three grain sizes. Activation enthalpies 400–440 kJ/mol (4.2–4.6 eV). (b) Stress dependence of the steady-state creep rate at three temperatures. Mean stress exponent: $n = 1.1$.
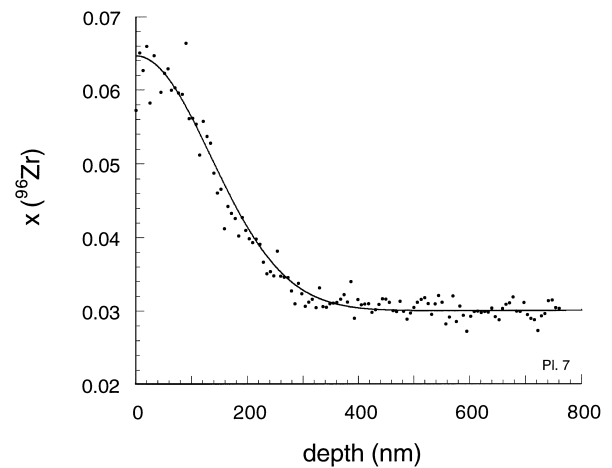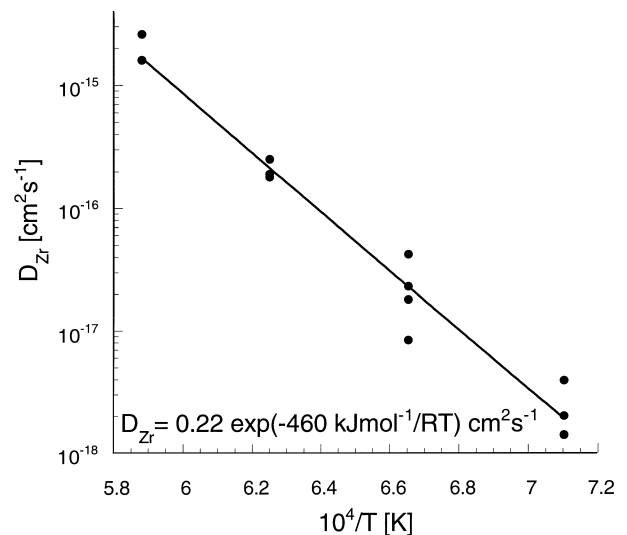

Fig. 12. Temperature dependence of the zirconium tracer diffusivity. The Arrhenius fit yields an activation energy of 460 kJ/mol (4.8 eV).
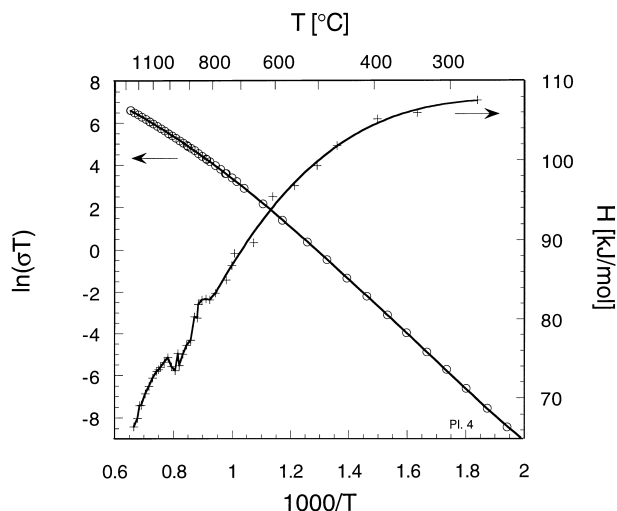
Fig. 13. Temperature dependence of the DC-conductivity and differentiated curve (apparent activation enthalpy H_{DC}). H_{DC} gradually decreases from 110 to 70 kJ/mol (1.1–0.7 eV).

for 484 h at 810°C, the conductivity decreased to about 75% of its initial value.

4. Discussion

The yttria content of this material is near the minimum required for full stabilization of the cubic phase[29,30] and precipitation of tetragonal or pseudo-cubic phase can occur at temperatures about 1000°C which are of interest as well for technological applications as for the present measurements. Effectively, although X-ray diffraction shows only cubic reflections (Fig. 3), TEM-SAD revealed forbidden reflections in several grains [Fig. 4(c)], characteristic of the tetragonal phase. This could be due to the formation of small tetragonal precipitates during cooling following sintering, which would, however, be of nanometric size [Fig. 4(b)]. The present results are thereby similar to those reported on materials of same composition.[29,31] No domain contrast of t′-phase was obtained, again in accordance to what is expected for a material containing > 7.5 mol% Y_2O_3.[31]

The microstructural changes accompanying thermal treatments of this type of materials are still unclear. Neither the relevant part of the equilibrium phase diagram has been unambiguously established,[12] nor has there been sufficient proof as to the identity of ordered microdomains. In the present case, the Raman spectrum of samples annealed for 100 days at 1150°C shows features both arising from the cubic and the tetragonal phase, thereby confirming that at this temperature the cubic phase is not stable, while after annealing at 1460 and 1700°C only the cubic phase is observed, in agreement with the phase diagram given by Stubican.[10] However, the kinetics of precipitation of tetragonal

phase are slow and in the time scale (hours) of the present experiments (mechanical loss, creep, conductivity) the material can be considered as cubic.

Diffuse electron scattering was observed [Fig. 4(c and d)] which is a typical feature of the diffraction patterns of several cubic zirconias.[32–35] The origin of this phenomenon has not yet been established: it could be due to ordered microdomains or to local ordering of oxygen vacancies.

The damping properties of this material are characterized by a double anelastic relaxation maximum at low temperatures (< 600°C), followed by a range of low damping and then, at high temperature (> 900°C), a steady increase of damping of viscoelastic type. Maximum I is equivalent to the maximum I observed in all zirconia materials, tetragonal[36,37] as well as cubic.[38,39] It has been attributed to the reorientation of elastic dipoles $(Y'_{Zr} V_{\ddot{O}})^{\cdot}$ formed between dopant cations and oxygen vacancies. Its activation enthalpy of about 135 kJ/mol (1.4 eV) is consistent with the dependence of the activation enthalpy values determined for maximum I as a function of yttrium content.[39] As for the satellite maximum (I_B), it does not seem to follow the scheme obtained for the satellite maxima (termed I_A elsewhere)[38,39] obtained for fully stabilized cubic zirconia single crystals with higher yttria concentration. One obvious reason for this behaviour could be the presence of grain boundaries. However, such a maximum does not occur at all in tetragonal zirconia polycrystals (2Y-TZP, 3Y-TZP),[37] which contain a much higher proportion of grain boundaries. Moreover, the present material is rather pure (Table 1) compared to some of the TZP materials mentioned. Another possible explanation for this maximum could be the presence of small tetragonal precipitates or ordered microdomains, creating damping interfaces. Indeed, a satellite maximum was observed in ZrO_2-4 mol% Y_2O_3[37] which, moreover, grew after thermal treatments susceptible to allow precipitation and growth of tetragonal phase in these partially stabilized materials. After annealing for 484 h at 810°C, the satellite maximum I_B markedly decreases, thus manifesting an evolution of the microstructure. Similar behaviour was reported recently[40] where this phenomenon is attributed to the local ordering of oxygen vacancies during ageing. More detailed investigations of the relaxation properties of the satellite maximum are under way in order to identify the underlying mechanism.

The ionic conductivity of this material is in close agreement with a similar material studied by Ciacchi et al.[3] The continuous change in slope between low and high temperature (Fig. 13), corresponding to a change of activation enthalpy from 110 kJ/mol (1.1 eV) to 70 kJ/mol (0.7 eV), is in accordance with the oxygen vacancy-association model.[1] The low temperature value is, however, significantly lower than that for dipole reorientation obtained for mechanical loss (see maximum I, 1.4 eV). Above 800°C, the conductivity shows

anomalous behaviour, which appears more clearly on the derived curve (activation enthalpy). With higher dopant content, such effects are even more pronounced and are pointing to an order-disorder transition.[41,42] Effectively, after annealing for 484 h at 810°C, the conductivity drops to about 75% of its initial value, in close agreement with Kondoh et al.[43] who attributed this aging effect to short range ordering of oxygen vacancies.

The obtained value for the dynamical Young's modulus (200 GPa at low temperature) agrees well with the elastic Young's modulus calculated from single crystal elastic constants ($\approx$233 GPa).[44] The slightly lower value could be due to differences in density between nearly fully dense sintered materials and a single crystal, as suggests the increase of modulus in the intermediate temperature range.

The high temperature viscoelastic damping depends on cation motion, as is suggested by the associated high activation enthalpy of 530 kJ/mol (5.5 eV). This value is a little higher than the ^{96}Zr tracer diffusion activation energy of 460 kJ/mol (4.8 eV). Viscoelastic damping could, e.g. arise from the glide/climb motion of intragranular dislocations or from grain boundary sliding. In the latter case, the activation enthalpy should be equal to that for grain-boundary cation diffusion. For the present material, however, no reliable data exist on grain boundary diffusion. As to the broadening factor of $\alpha = 0.3$ obtained for the viscoelastic damping background, it is of the same order as found for other ceramic materials.[28,45,46]

The obtained creep exponent of $n \approx 1$ is typical for diffusional creep. The grain size parameter of $p = 2.5$ lies between the values for Nabarro-Herring creep ($p = 2$, creep controlled by intragrain diffusion[47,48]) and Coble creep ($p = 3$, creep controlled by intergranular diffusion[49]). However, if the materials parameters are inserted into these two models, a much better agreement is found for the Nabarro-Herring model. The experimental creep rate at 1200°C, 75 MPa is $5.8 \cdot 10^{-9}$ s^{-1}, which is very close to the value of $1.3 \cdot 10^{-9}$ s^{-1} predicted by the Nabarro-Herring model, while the Coble model predicts a much slower rate ($2.7 \cdot 10^{-16}$ s^{-1}). Nevertheless, other grain boundary sliding models can lead to comparable predicted creep rate values. Extensive SEM studies on crept samples would be needed to obtain further information as to the creep mechanism. As for the activation enthalpy, the values obtained at 75 MPa for the investigated grade are 440 kJ/mol, i.e. close to the one for intragranular cation diffusion (460 kJ/mol). Comparable creep behaviour of cubic polycrystalline zirconia has been reported, where diffusional creep also seems to prevail. In some cases[13] similar and in others[16–18] higher values of the creep activation enthalpy were reported.

The measured ^{96}Zr tracer diffusion activation energy of 460 kJ/mol (4.8 eV) agrees well with the values reported in the literature.[4,6,50] Because the investigated material has a grain size which is much larger than the diffusion length, no evidence of grain boundary contribution to the diffusion profiles was found. The values obtained are therefore believed to be representative of the grain interior. There is no significant influence of the preparation conditions on the zirconium tracer diffusion. The large values of the entropy of motion ($\gg$5 k$_B$) are at present inexplicable along classical guidelines. According to the current models,[51] this entropy should not be higher than 3 k$_B$.

5. Conclusions

In the present investigation, identical ZrO$_2$-8 mol%Y$_2$O$_3$ polycrystals were characterized as to their microstructure, mechanical properties, cation diffusion and ionic conductivity by using various complementary experimental techniques in the framework of a joint research programme.

The obtained microstructural features are in agreement with those reported for similarly doped materials and the materials are highly pure. At low temperature, two mechanical relaxation processes take place, the first one attributed to the reorientation of elastic dipoles $(Y'_{Zr} V_O^{\cdot\cdot})^{\cdot}$ and the second one related to ageing. The DC-conductivity of these materials is as expected from literature. Moreover, well resolved measurements of the temperature dependence of the conductivity revealed anomalous behaviour above 800°C, indicating the occurence of the order–disorder transition.

At high-temperature, the investigated mechanical properties (viscoelastic damping, creep resistance) are both controlled by cation diffusion, as suggested by the activation enthalpy values obtained by mechanical spectroscopy, creep tests and diffusion experiments. High temperature damping was measured for the first time in these materials and shows a viscoelastic-type increase of damping above 1000°C, revealing the onset of non-recoverable defect motion. This is effectively followed by creep at higher stress and temperature. The obtained creep parameters of $n \approx 1$ and $p \approx 2.5$ indicate Nabarro-Herring creep as the rate-controlling mechanism.

References

1. Badwal, S. P. S., Ceramic superionic conductors. In *Structure and Properties of Ceramics, Vol. 11, Materials Science and Technology*, ed. M. V. Swain. VCH, Weinheim, Germany, 1994, pp. 567–633.

2. *Proceedings of the Third International Meeting on Solid Oxide Fuel Cells*, ed. S. C. Singhal and H. Iwahara. The Electrochemical Society Inc., Pennington, NJ, 1993.

3. Ciacchi, F. T., Crane, K. M. and Badwal, S. P. S., Evaluation of commercial zirconia powders for solid oxide fuel cells. *Solid State Ionics*, 1994, **73**, 49–61.

4. Solmon, H., Chaumont, J., Dolin, C. and Monty, C., Zr, Y and O self diffusion in $Zr_{1-x}Y_xO_{2-x/2}$ ($x = 0.17$). *Ceram. Trans.*, 1991, **24**, 175–184.

5. Chien, F. R. and Heuer, A. H., Lattice diffusion kinetics in Y_2O_3-stabilized cubic ZrO_2 single crystals: a dislocation loop annealing study. *Phil. Mag. A*, 1996, **73**, 681–697.

6. Kilo, M., Borchardt, G., Weber, S., Scherrer, S. and Tinschert, K., Zirconium and calcium tracer diffusion in stabilized cubic zirconia. *Ber. Bunsenges. Phys. Chem.*, 1997, **101**, 1361–1365.

7. Cannon, W. R. and Langdon, T. G., Review. Creep of ceramics. Part 1. Mechanical characteristics. *J. Mater. Sci.*, 1983, **18**, 1–50.

8. Suzuki, Y., Activation energy for electrical conduction of Y_2O_3-stabilized zirconia containing 8 mol% Y_2O_3. *Solid State Ionics*, 1996, **91**, 239–241.

9. Yoshimura, M., Phase stability of zirconia. *Ceram. Bull.*, 1988, **67**, 1950–1955.

10. Stubican, V. S., Phase equilibria and metastabilities in the systems ZrO_2-MgO, ZrO_2-CaO and ZrO_2-Y_2O_3. In *Advances in Ceramics, Vol. 24, Science and Technology of Zirconia III*, ed. S. Somiya, N. Yamamoto and H. Yanagida. The American Ceramic Society, 1988, pp. 71–82.

11. Murakami, Y., Nagano, I. and Yamamoto, H., Phase equilibria and phase change during ageing in the ZrO_2-Y_2O_3 system. *J. Mater. Sci. Lett.*, 1997, **16**, 1686–1688.

12. Yashima, M., Kakihana, M. and Yoshimura, M., Metastable-stable phase diagrams in the zirconia-containing systems utilized in solid-oxid fuel cell application. *Solid State Ionics*, 1996, **86–88**, 1131–1149.

13. Evans, P. E., Creep in yttria- and scandia-stabilized zirconia. *J. Am. Ceram. Soc.*, 1970, **53**, 365–369.

14. Fehrenbacher, L. L., Bailey, F. P. and McKinnon, N. A., Compressive creep of yttria rare earth stabilized zirconia storage heater refractories. *SAMPE Q.*, 1971, **2**, 18–30.

15. Seltzer, M. S. and Talty, P. K., Creep of low-density yttria/rare earth-stabilized zirconia. In *Proceedings of the Conference on Deformation of Ceramic Materials*, ed. R. C. Bradt and R. E. Tressler. Plenum Press, 1975, pp. 297–312.

16. Seltzer, M. S. and Talty, P. K., High-temperature creep of Y_2O_3-stabilized ZrO_2. *J. Am. Ceram. Soc.*, 1975, **58**, 124–130.

17. Dimos, D. and Kohlstedt, D. L., Diffusional creep and kinetic demixing in yttria-stabilized zirconia. *J. Am. Ceram. Soc.*, 1987, **70**, 531–536.

18. Bravo-León, A., Jiménez-Melendo, M. and Domínguez-Rodríguez, A., Mechanical and microstructural aspects of the high temperature plastic deformation of yttria-stabilized zirconia polycrystals. *Acta Metall. Mater.*, 1992, **40**, 2717–2726.

19. Wakai, F., Sakaguchi, S. and Matsuno, Y., Superplasticity of yttria-stabilized tetragonal zirconia polycrystals. *Adv. Ceram. Mater.*, 1986, **1**, 259–263.

20. Tekeli, S. and Davies, T. I., Influence of a transition metal oxide (CuO) on the superplastic behaviour of 8 mol% yttria-stabilised cubic zirconia polycrystal (8Y-CSZ). *J. Mater. Sci.*, 1998, **33**, 3267–3273.

21. Görke, O., Kriechuntersuchungen an kubischen ZrO_2-Legierungen. Diploma-Thesis. Technische-Universität Berlin, 1997.

22. Weller, M. and Wert, C., Neue physikalische Untersuchungen zur Struktur der Moleküle im Bernstein. *Stuttgarter Beiträge zur Naturkunde, Bernstein-Neuigkeiten*, 1984, **C18**, 85–100 (Staatliches Museum für Naturkunde, Stuttgart, Germany).

23. Weller, M. and Török, E., Automatic system for measurements of internal friction and elastic moduli. *J. Phys. (France)*, 1987, **C8**, 371–376.

24. Weller, M., Characterization of high purity bcc metals by mechanical spectroscopy. *J. Phys. (France)*, 1995, **C7**, 199–204.

25. Nowick, A. S. and Berry, B. S., *Anelastic relaxation in crystalline solids*. Academic Press, New York and London, 1972.

26. Schoeck, G., Bisogni, E. and Shyne, J., The activation energy of high-temperature internal friction. *Acta Metall.*, 1964, **12**, 1466–1468.

27. Crank, J., *The Mathematics of Diffusion*. Oxford University Press, Oxford, 1957.

28. Lakki, A., Schaller, R., Carry, C. and Benoit, W., High temperature anelastic and viscoplastic deformation of fine-grained MgO-doped Al_2O_3. *Acta Mater.*, 1998, **46**, 689–700.

29. Rühle, M., Claussen, N. and Heuer, A. H. Microstructural studies of Y_2O_3-containing tetragonal ZrO_2 polycrystals (Y-TZP). In *Advances in Ceramics, Vol. 12, Science and Technology of Zirconia II*, ed. N. Claussen, M. Rühle and A. H. Heuer. The American Ceramic Society, Columbus, Ohio, 1984, pp. 352–370.

30. Suzuki, Y., Phase transition temperature of fluorite-type ZrO_2-Y_2O_3 solid solutions containing 8–44 mol% Y_2O_3. *Solid State Ionics*, 1995, **81**, 211–216.

31. Zhou, Y., Lei, T. C. and Sakuma, T., Diffusionless cubic-to-tetragonal phase transition and microstructural evolution in sintered zirconia-yttria ceramics. *J. Am. Ceram. Soc.*, 1991, **74**, 633–640.

32. Dai, Z. R. and Wang, Z. L., Local ordering of oxygen vacancies in cubic zirconia (ZrO_2) stabilized with yttria (Y_2O_3) and magnesia (MgO). I. Electron diffuse scattering study. *Phil. Mag. A*, 1996, **73**, 415–430.

33. Chaim, R. and Brandon, D. G. Short-range order phenomena in ZrO_2 solid solutions. In *Advances in Ceramics, Vol. 12, Science and Technology of Zirconia II*, ed. N. Claussen and M. Rühle and A. H. Heuer. The American Ceramic Society, Columbus, Ohio, 1984, pp. 86–95.

34. Marder, J. M., Mitchell, T. E. and Heuer, A. H., Precipitation from cubic ZrO_2 solid solutions. *Acta Metall.*, 1983, **31**, 387–395.

35. Kondoh, J., Kikuchi, S., Tomii, Y. and Ito, Y., Effect of aging on yttria-stabilized zirconia. II. A study of the effect of the microstructure on conductivity. *J. Electrochem. Soc.*, 1998, **145**, 1536–1550.

36. Weller, M. and Schubert, H., Internal friction, dielectric loss and ionic conductivity in ZrO_2-3%Y_2O_3 (Y-TZP). *J. Am. Ceram. Soc.*, 1986, **69**, 573–577.

37. Weller, M., Schubert, H. and Kountouros, P. Mechanical and dielectric loss measurements in Y_2O_3-ZrO_2 and TiO_2-Y_2O_3-ZrO_2 ceramics. In *Science and Technology of Zirconia*, S. P. S. Badwal, M. J. Bannister and R. H. J. Hannink. Technomic Publ. Co, Lancaster and Basel, 1993, pp. 546–554.

38. Weller, M., Atomic defects in yttria- and calcia-stabilized zirconia. *Z. Metallkd.*, 1993, **84**, 381–386.

39. Weller, M. and Lakki, A., Defects in cubic zirconia studied by mechanical loss spectroscopy. *Ber. Bunsenges. Phys. Chem.*, 1997, **101**, 1297–1302.

40. Kondoh, J., Kikuchi, S., Tomii, Y. and Ito, Y., Effect of aging on yttria-stabilized zirconia. III. A study of the effect of local structures on conductivity. *J. Electrochem. Soc.*, 1998, **145**, 1550–1560.

41. Gibson, I. R. and Irvine, J. T. S., Study of the order-disorder transition in yttria-stabilized zirconia by neutron diffraction. *J. Mater. Chem.*, 1996, **6**, 895–898.

42. Herzog, R., Lakki, A. and Weller, M., to be published.

43. Kondoh, J., Kawashima, T., Kikuchi, S., Tomii, Y. and Ito, Y., Effect of aging on yttria-stabilized zirconia. I. A study of its electrochemical properties. *J. Electrochem. Soc.*, 1998, **145**, 1527–1536.
44. Kandil, H. M., Greiner, J. D. and Smith, J. F., Single-crystal elastic constants of yttria-stabilized zirconia in the range 20–700°C. *J. Am. Ceram. Soc.*, 1984, **67**, 341–346.
45. Lakki, A., Schaller, R., Bernard-Granger, G. and Duclos, R., High temperature anelastic behaviour of silicon nitride studied by mechanical spectroscopy. *Acta Metall. Mater.*, 1995, **43**, 419–426.
46. Lakki, A., Schaller, R., Nauer, M. and Carry, C., High temperature superplastic creep and internal friction of yttria doped zirconia polycrystals. *Acta Metall. Mater.*, 1993, **41**, 2845–2853.
47. Herring, C., Diffusional viscosity of a polycrystalline solid. *J. Appl. Phys.*, 1950, **21**, 437–445.
48. Nabarro, F. R. N., Deformation of crystals by the motion of single ions. In *Proceedings of the Conference on the Strength of Solids*, 1948. The Physical Society, London, pp. 75–90.
49. Coble, R. L., A model for boundary diffusion controlled creep in polycrystalline materials. *J. Appl. Phys.*, 1963, **34**, 1679–1682.
50. Oishi, Y., Ando, K. and Sakka, Y., Lattice and grain-boundary diffusion coefficients of cations in stabilized zirconias. In *Adv. in Ceramics*, ed. M. F. Yan and A. H. Heuer. Am. Ceram. Soc., pp. 208–219.
51. Philibert, J., *Atom Movements: Diffusion, Transport in Solids, Les Editions de Physique*. Les Ulis, France, 1991.